Resonant and Off-Resonant Magnetoacoustic Waves in Epitaxial Fe_3Si/GaAs Hybrid Structures

Marc Rovirola,[1,2,*] M. Waqas Khaliq,[1,3] Blai Casals,[2,4] Michael Foerster,[3] Miguel Angel Niño,[3] Lucía Aballe,[3] Jens Herfort,[5] Joan Manel Hernàndez,[1,2] Ferran Macià,[1,2,†] and Alberto Hernández-Mínguez[5,‡]

[1] *Dept. of Condensed Matter Physics, University of Barcelona, 08028 Barcelona, Spain*
[2] *Institute of Nanoscience and Nanotechnology (IN2UB), University of Barcelona, 08028 Barcelona, Spain*
[3] *ALBA Synchrotron Light Source, 08290 Cerdanyola del Vallès, Spain*
[4] *Dept. of Applied Physics, University of Barcelona, 08028 Barcelona, Spain*
[5] *Paul-Drude-Institut für Festkörperelektronik, Leibniz-Institut im Forschungsverbund Berlin e.V., Hausvogteiplatz 5–7, 10117 Berlin, Germany*

(Received 16 December 2022; revised 1 June 2023; accepted 22 August 2023; published 22 September 2023)

Surface acoustic waves (SAWs) provide an efficient dynamical coupling between strain and magnetization in micro- and nanometric systems. Using a hybrid device composed of a piezoelectric, GaAs, and a ferromagnetic Heusler alloy thin film, Fe_3Si, we are able to quantify the amplitude of magnetoacoustic waves generated with SAWs via magnetic imaging in an x-ray photoelectron microscope. The cubic anisotropy of the sample, together with a low damping coefficient, allows for the observation of resonant and nonresonant magnetoelastic coupling. Additionally, via micromagnetic simulation, we verify the experimental behavior and quantify the magnetoelastic shear strain component in Fe_3Si, which appears to be large ($b_2 = 10 \pm 4$ MJm^{-3}).

DOI: 10.1103/PhysRevApplied.20.034052

I. INTRODUCTION

The use of charge carriers for information transport has proven to be successful, but current technology is reaching its limitations and the growing need for smaller, faster, and more efficient information processing units calls for new data carriers. One of the solutions compatible with existing technology and involving low-energy dissipation are spin waves—collective excitation of magnetic order. However, the generation, detection, and manipulation of spin waves are still the focus of many studies due to the multiple interactions that these magnetization modes have with other degrees of freedom such as phonons or photons [1,2].

The coupling between strain and magnetization—the magnetoelastic (ME) effect—can be used to generate magnetization dynamics at the nanoscale with low-power dissipation through surface acoustic waves (SAWs) [3–9]. The interaction between SAWs and magnetization dynamics has long been studied [9–19] and there are clear experiments showing the variation of magnetic states caused by SAWs. Conversely, changes in SAW propagation are observed due to the action of magnetization dynamics. SAW-induced magnetization waves, including magnetoacoustic switching, typically occur at magnetic resonances [4,12–15,17,20]. Nonresonant driving of magnetic excitations by SAWs have also been used for fast magnetization switching of Co bars, pinning of domain walls in ferromagnetic nanowires, and assisted nucleation of skyrmions [19]. However, there is no clear picture of what type of magnetoacoustic waves might be generated, if any, when magnetic and acoustic systems are in a nonresonance condition. Therefore, imaging techniques capable of quantifying both SAW and magnetization dynamics are required to fully explore the interaction between these excitation modes in both resonant and nonresonant conditions.

The coherent transport of spin waves up to micrometers is a requirement for processing units and for that reason finding materials with low damping coefficients is critical. Materials such as nickel have a large ME effect, which makes them ideal for generating strain-induced spin waves, but they display a large damping coefficient of the order of 10^{-2} [21] causing short propagation distances and broad resonance peaks. In contrast, yttrium iron garnet has a damping coefficient on the order of 10^{-4} [22], but high-quality growth is challenging and it is a weak magnetoelastic material. Epitaxial Heusler alloys are promising alternatives due to their low spin-wave damping, half-metallicity, and compatibility with CMOS

*marc.rovirola@ub.edu
†ferran.macia@ub.edu
‡alberto.h.minguez@pdi-berlin.de

technology [23–29]. Specifically, $Fe_{1-x}Si_x$ films grown epitaxially on GaAs have been reported to have a damping coefficient as low as 3×10^{-4} [30] and magnetoelastic constant as high as $b_2 = 7$ MJm^{-3}, for a Si concentration of $x = 25\%$ [31,32].

In this paper we study the acoustic excitation of spin waves in samples consisting of a piezoelectric GaAs substrate with interdigital transducers (IDTs) for the generation of SAWs, and a ferromagnetic Fe_3Si thin film on the SAW acoustic path (see Fig. 1). The high structural quality of Fe_3Si leads to very narrow ferromagnetic resonance (FMR) peaks, indicative of low Gilbert damping ($\alpha \simeq 0.005$) and, therefore to a large coherence length of the spin wave. To quantify the spin waves, direct imaging through x-ray microscopy of both SAWs and magnetization waves is taken at different magnetic fields, demonstrating that magnetoacoustic waves are generated in a wide range of fields, and showing that resonance is not an essential condition to generate magnetoacoustic waves.

The paper is organized as follows. Section II describes the sample fabrication process and the experimental procedures. Section III is divided into two parts: first, experimental results, beginning with the characterization of the sample via FMR and SAW transmission, and then analysis of direct imaging of both SAWs and magnetic waves; and second, micromagnetic simulations further verifying and quantifying magnetoelastic constants of the sample and supporting the result that magnetoacoustic waves can also exist in nonresonance conditions. Section IV presents conclusions on the results.

II. EXPERIMENTAL DETAILS

The studied sample is a 74-nm-thick $Fe_{1-x}Si_x$ film with $x = 25\%$ Si content grown by molecular beam epitaxy on a piezoelectric, GaAs (001) [23]. The fabrication of the magnetoacoustic device begins by selective patterning of the Fe_3Si film into cross-shaped structures by electron beam lithography and plasma etching. Pairs of IDTs are deposited on opposite sides of the patterned Fe_3Si film by electron beam lithography, metal evaporation, and liftoff (see Fig. 1), thus allowing for both the generation of SAWs propagating along the Heusler film and the measurement of transmitted SAW power (S_{21}) along the acoustic path. Figure 1(b) displays the S_{21} spectrum measured with a vector network analyzer. The IDTs are designed to excite Rayleigh SAWs [33,34] with a frequency of $f_{SAW} = 500$ MHz and corresponding wavelength $\lambda_{SAW} = 5.73$ μm propagating along the $X \parallel [110]$ direction of the GaAs substrate. Due to the high structural quality of the Fe_3Si film, the magnetization displays cubic in-plane anisotropy, with easy and hard axes being the families of ⟨100⟩ and ⟨110⟩ planes, respectively. Therefore, the SAWs propagate along one of the hard axes of the Fe_3Si film, and

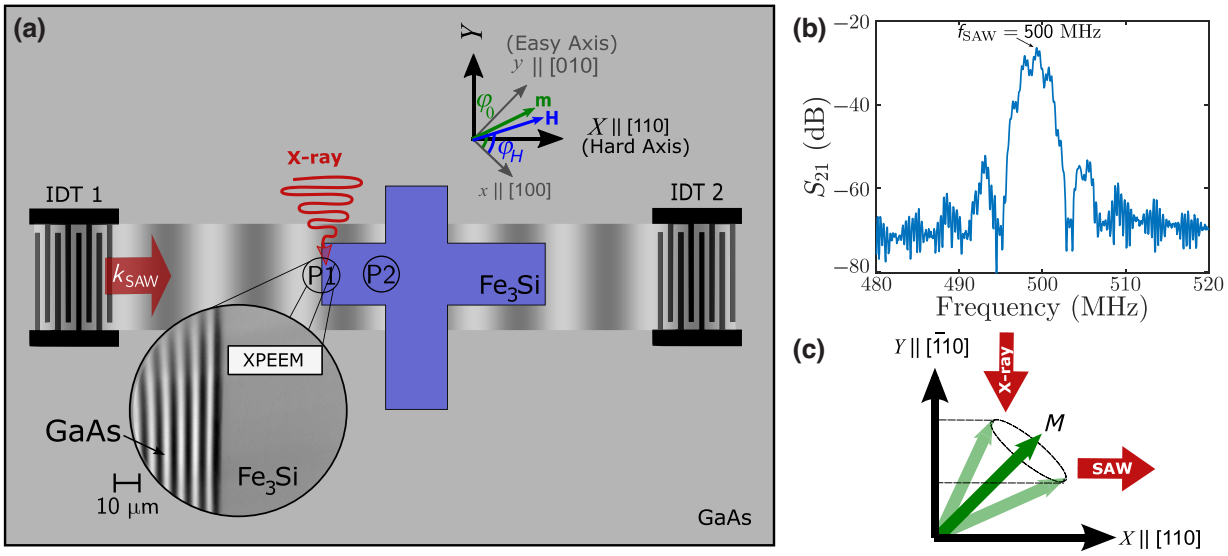

FIG. 1. (a) Schematic setup of the hybrid device, where a cross-shaped Heusler alloy film (Fe_3Si) is deposited on top of a GaAs substrate with interdigital transducers (IDTs) on both sides. The top right corner shows the coordinates of the sample, where x and y are the easy axes, while X and Y are the hard axes and show the equilibrium magnetization angle, φ_0, and the magnetic field, $\varphi_H = \pi/4 + \Delta\varphi_H$, with respect to the easy axis $x \parallel [100]$. An rf signal of 500 MHz is sent to IDT 1 to excite SAWs in the [110] direction and the x-rays are sent perpendicular to the SAW propagation direction. (b) Transmission coefficient between the two IDTs, S_{21}, as a function of the rf frequency, applied to IDT 1. The arrow points to the highest transmission and fundamental frequency of IDT 1 at 500 MHz. (c) Schematic representation of the magnetization precession in the Fe_3Si film with the SAW propagating in the X direction and the x-rays in the Y direction. The dashed lines that stretch in the Y direction show the magnetic signal that is captured by XMCD imaging.

magnetization in the absence of a magnetic field lies along any of the four easy axes forming a 45° angle with the SAW path. Rayleigh SAWs are characterized by longitudinal in-plane and out-of-plane strains ϵ_{XX} and ϵ_{ZZ}, respectively, as well as shear strain ϵ_{XZ}. The magnetoelastic effect transforms these varying strain components into a dynamic effective magnetic field in the Fe_3Si film, which results in the excitation of magnetoacoustic waves [35].

To image the sample, we used an x-ray photoemission electron microscope (XPEEM) at the CIRCE beamline at ALBA Synchrotron with a time and spatial resolution below 80 ps and 100 nm, respectively. The SAW frequency is synchronized to the repetition rate of the x-ray pulses, and the SAW and magnetization images are taken simultaneously [3,7,36,37]. The sample was mounted on a holder containing an electromagnet that can generate an in-plane magnetic field up to 20 mT with a variable angle. In our study, the magnetic field is applied close to the SAW propagation direction, i.e., $\varphi_H = \pi/4 + \Delta\varphi_H$ with respect to the [100] direction [see Fig. 1(a)]. Sending a radio frequency (rf) signal of the appropriate frequency to IDT 1 generates SAWs in GaAs that excite spin waves in the Fe_3Si with the same wavelength and frequency. When the sample and the electron microscope are kept at a large potential difference, electrons leaving the sample due to x-rays are accelerated toward the electron detector, where the number of electrons captured from each position on the sample depends on the amplitude of the piezoelectric field accompanying the SAW [37]. This allows us to obtain contrast images that are sensitive to SAW wavefronts at the GaAs surface, as seen in the inset of Fig. 1. In contrast, no SAWs can be detected in Fe_3Si due to its metallic nature—free charge carriers shield the dynamic piezoelectric field. However, the effect of the SAWs on the magnetization dynamics in the Fe_3Si can be imaged using x-ray magnetic circular dichroism (XMCD), which involves subtracting two otherwise identical XPEEM images taken with x-rays of opposite circular polarization [38].

III. RESULTS

A. Experimental results

The sample was initially characterized via FMR with a broadband coplanar waveguide capable of producing microwave magnetic fields with frequencies up to 20 GHz [39]. Figure 2 shows the resonance fields for the uniform precession mode (spin wave with $\mathbf{q} = 0$) when an in-plane magnetic field is applied in the [110] direction (hard axis). On top of the data, we plotted solid and dashed lines calculated from a macrospin model that includes fourfold crystalline anisotropy, shape anisotropy, and the external magnetic field with a deviation angle $\Delta\varphi_H$ from the [110] axis (see Refs. [29,35]). We notice here that the curve corresponding to a magnetic field direction that slightly deviates by $\Delta\varphi_H \simeq 2°$ from the [110] axis fits

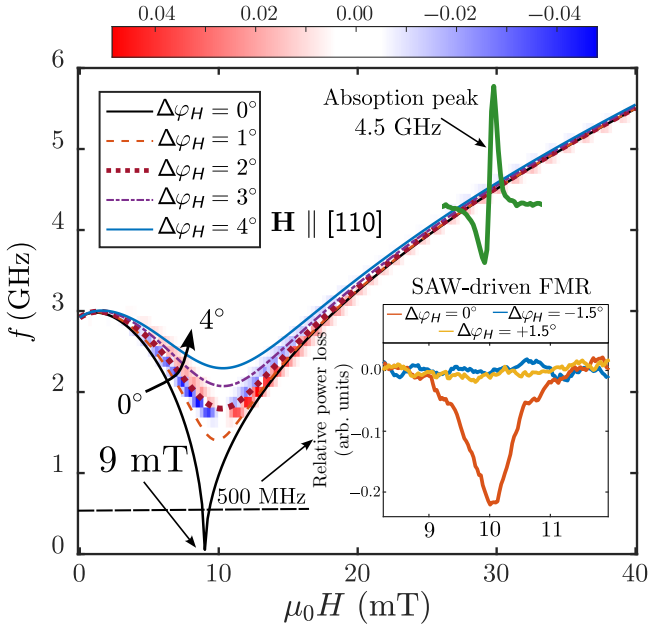

FIG. 2. FMR for a magnetic field applied along the [110] crystalline direction (hard axis) with the modeling curves plotted on top as continuous, dashed, and dotted lines for different deviation angles of the magnetic field, $\Delta\varphi_H$. The horizontal dashed line corresponds to the SAW frequency and the arrow points to the anisotropy field (9 mT) obtained from the model. The green curve at 4.5 GHz displays the absorption peak in the form of a Lorentzian derivative. The inset shows the variation of the SAW attenuation for $f_{SAW} = 500$ MHz as a function of the magnetic field strength for different field angles, $\Delta\varphi_H$ between SAW and H.

well the experimental data. The curve corresponding to a perfectly aligned magnetic field, $\Delta\varphi_H = 0°$ (continuous black curve), clearly shows the magnetic field required to suppress the in-plane anisotropy field, $\mu_0 H_k = 9$ mT, and align the magnetization along the hard axis. We also measured the linewidth broadening as a function of microwave frequency and found a value for the Gilbert damping coefficient, $\alpha = 0.005$ [40], an order of magnitude smaller than for nickel [21].

We also plotted in Fig. 2 a horizontal dashed line representing the frequency used in the SAW experiment (500 MHz). The crossing points between the FMR curves and the dashed line indicate the magnetic fields at which the magnetization of the Fe_3Si film is at resonance with the SAW frequency. Notice that a slight deviation of the magnetic field ($\Delta\varphi_H \neq 0$) and the fact that the SAW excites spin waves with $\mathbf{q} \neq 0$ can shift the resonance condition to slightly larger magnetic fields [41].

To characterize further our hybrid structures, we measured the change in SAW attenuation as a function of the magnetic field strength (see the inset of Fig. 2). Measurement of power transmission, S_{21}, between two opposite IDTs serves to investigate the resonant ME coupling

between SAW and spin waves in our Heusler thin film. Similarly to FMR measurements, there is a sharp transmission dip with a linewidth of approximately 1 mT, caused by the additional transfer of energy between SAW and magnetization under resonance conditions. This resonance dip shows a strong angular dependence already reported for epitaxial Fe thin film in GaAs by Duquesne in Ref. [42] and Rovillain in Ref. [43]. In our case, a deviation of $\Delta\varphi_H = \pm 1.5^\circ$ of the magnetic field direction with respect to the [110] axis results in no measurable power loss associated to the magnetoelastic resonance (see Fig. 2 inset).

Next, we turn to the main experimental results consisting of resolving in space and time the evolution of magnetoacoustic waves in the Heusler film. First, we characterized the strength of a 500-MHz SAW by direct XPEEM images of the GaAs substrate. The observed SAW wave fronts in the XPEEM image (see the left-hand side of the inset in Fig. 1) are associated with the energy shift of secondary electrons leaving the sample surface of GaAs due to the piezoelectric field of the SAW. The energy shift can be quantified by a local photoelectron kinetic energy scan [37]—photoemission intensity as a function of the electron kinetic energy. The shift between both spectra taken at the wave edges (the difference between maxima and minima) corresponds to the peak-to-peak value and was found to be $V_{\text{p.p.}} = 0.1$ V. By numerically solving the coupled elastic and electromagnetic equations for a SAW propagating along the [110] axis of GaAs [37], we estimate that the measured piezoelectric amplitude of $V_0 \approx V_{\text{p.p.}}/2 \approx 0.05$ V at the surface of the GaAs substrate corresponds to strain components with amplitudes $\varepsilon_{XX} = 3.6 \times 10^{-5}$, $\varepsilon_{ZZ} = 2.3 \times 10^{-5}$ and $\varepsilon_{XZ} = 7.4 \times 10^{-7}$ at about 30 nm depth of the Fe_3Si film (which corresponds to half the film thickness). This is almost one order of magnitude smaller than the same quantity measured in $LiNbO_3$ piezoelectric structures under similar SAW frequencies [3,7].

To obtain XMCD images that are proportional to the Fe_3Si magnetization component along the x-ray incidence direction, we selected the x-ray energy for the L_3 absorption edge of Fe [38]. In our experiment, the x-ray incidence is along the hard axes (Y axis) perpendicular to the SAW propagation direction [see Fig. 1(c)]. Figure 3(a) shows an XMCD image revealing magnetic domains in all four easy axis directions with a strong contrast that allows us to quantify the overall change in magnetization in the x-ray direction.

The generation of SAWs in GaAs creates a dynamic strain in the Fe_3Si film that induces a time-varying magnetic anisotropy, which leads to the excitation of magnetoacoustic waves. Their amplitude can be seen in the XMCD image, but with contrast between one or two orders of magnitude lower than the magnetic domains observed in Fig. 3(a). Figure 3(b) displays an XMCD image under a magnetic field of $\mu_0 H \simeq 10$ mT, showing magnetoacoustic

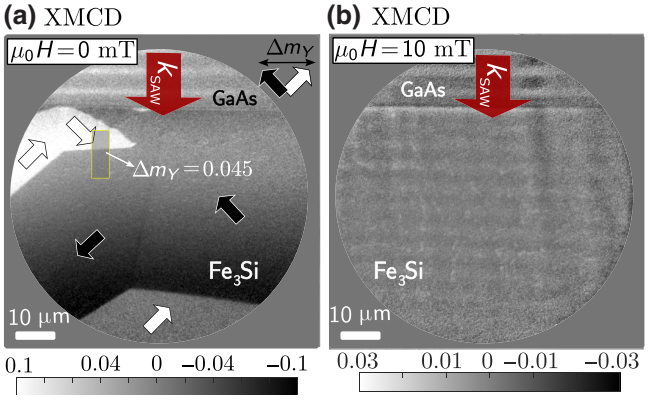

FIG. 3. (a) XMCD image of the magnetic domains in Fe_3Si and of the SAW in the GaAs. The magnetization direction of each domain is represented by white and black arrows. The difference between opposing magnetic states is represented by Δm_Y. (b) XMCD image with SAW in the GaAs and spin waves in Fe_3Si.

waves in the Fe_3Si film (there are no magnetic domains for applied fields larger than 1 mT). A remaining SAW signal in the GaAs is still visible, both in Figs. 3(a) and 3(b), due to tiny temperature drifts during integration time, which make the two XPEEM images taken for XMCD slightly different and thus not fully canceling out the SAW component.

To study the importance of magnetic resonance condition in the generation of magnetoacoustic waves, we measured XMCD images as a function of the applied magnetic field as was done in the FMR and SAW transmission characterization in Fig. 2. In the case of XPEEM, the maximum field used was 12 mT in order to avoid excessive image distortion. We took XMCD images in two different areas of the sample, P1 and P2, as shown in Fig. 1. Location P1 includes both the GaAs substrate and the Fe_3Si film as seen in Fig. 3(b). By fitting the magnetoacoustic wave profile to a sinusoidal function [44], we can retrieve the amplitude and quantify it with respect to the overall M_s value found in the magnetic domain image [45]. The normalized amplitude is showcased in Fig. 4 for the two areas and shows that there are sizable magnetoacoustic waves on a large magnetic field range with a sharp increase around 9–10 mT, which is exactly the magnetic resonance field for spin waves with $\mathbf{q} = \mathbf{k}_{\text{SAW}}$. Thus, magnetoacoustic waves are created with SAW even under nonresonance conditions. The constant SAW attenuation out of resonance does not result in a constant magnetization wave excitation, but rather creates a broad peak that depends on the effective magnetic field within the Fe_3Si film. When the effective field is low, the small amount of energy transferred from the SAW is enough to create a sizable magnetization wave, while when the effective field is large, there is no measurable magnetization wave. Our quantification of the

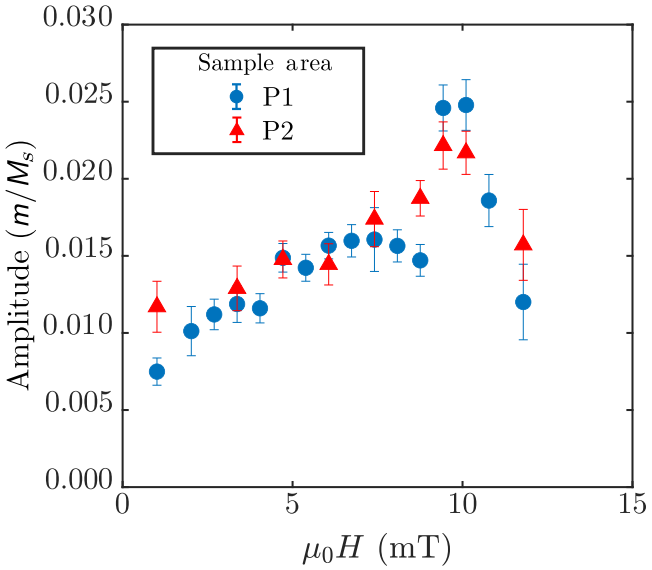

FIG. 4. Spin-wave amplitude obtained from the XMCD images as a function of the in-plane magnetic field at two different positions (P1, P2) of the sample as indicated in Fig. 1(a).

magnetoacoustic waves gives an estimate of 0.5–1.5° precession amplitude for the magnetization vector around the equilibrium.

The results of both sample locations are similar and are plotted in Fig. 4. Two parts can be identified: the first resembles a broad inverted parabola, and the second is a narrow peak of 1 mT width close to 9–10 mT. The first part corresponds to nonresonant magnetoacoustic excitation. In the absence of an applied magnetic field, the effective field associated with the cubic anisotropy keeps the magnetization along the in-plane easy axes of the Fe_3Si film [as seen in the XMCD image of Fig. 3(a)]. As the in-plane magnetic field increases, it generates a torque that partially counteracts the anisotropy, until it reaches the anisotropy field close to 9 mT. At this point, the total effective field is zero, so that the magnetization can easily respond to the periodic magnetic anisotropy modulation created by the SAW. Further increases of the magnetic field strength again locks the magnetization direction, so that oscillations around the equilibrium direction become smaller. The second part of the curve corresponds to resonance or near-resonance effects close to 9–10 mT. Here, the magnetization precession is enhanced due to the proximity of the spin-wave and acoustic wave frequencies, leading to the additional power losses observed in the FMR and SAW transmission experiments of Fig. 2.

B. Micromagnetic simulation

We performed micromagnetic modeling with MUMAX3 [46] to estimate magnetoelastic constants, b_1 and b_2, that couple the strain of the SAW with the magnetization of the Fe_3Si. The modeling accounts for all magnetic interactions, including dipolar, shape, and cubic anisotropies, as well as exchange interactions together with time and spatially oscillating strain fields associated with the SAW. We used the strain field amplitudes found in Sec. III A and the following values for the ferromagnetic Fe_3Si film found via FMR [40]: $M_s = 955 \times 10^3$ A/m, $A_{\rm ex} = 1 \times 10^{-11}$ J/m, $\alpha = 0.005$, and $K_{c1} = -4400$ J/m^3, where M_s is the saturation value of magnetization, $A_{\rm ex}$ is the exchange stiffness and K_{c1} is the first-order cubic anisotropy constant. The value of $A_{\rm ex}$ was calculated using the exchange stiffness constant $D = 240$ meV Å^2 [47] and the relation $A_{\rm ex} = DM_s/2g\mu_B$ where g is the Landé factor and μ_B is the Bohr magneton. The free energy of the magnetoelastic interaction [35,48] can be written as

$$F_{\rm ME} = b_1\left[\varepsilon_{xx}m_x^2 + \varepsilon_{yy}m_y^2 + \varepsilon_{zz}m_z^2\right] + 2b_2\left[\varepsilon_{xy}m_xm_y + \varepsilon_{xz}m_xm_z + \varepsilon_{yz}m_ym_z\right], \quad (1)$$

where the strain components ε_{ij}, and normalized magnetization components, m_i, with $i, j = (x, y, z)$ are expressed in the coordinate system with axes parallel to the $\langle 100\rangle$ directions of GaAs and Fe_3Si. The SAW strain components ε_{XX}, ε_{ZZ} and ε_{XZ}, expressed in the rotated frame with the X and Y axes parallel to the $\langle 110\rangle$ directions of GaAs and Fe_3Si, are related to the strain components in the coordinate system (x, y, z) using the following formulas:

$$\begin{aligned} \varepsilon_{xx} &= \varepsilon_{XX}\cos^2\varphi_{\rm SAW}, & \varepsilon_{xy} &= \varepsilon_{XX}\cos\varphi_{\rm SAW}\sin\varphi_{\rm SAW}, \\ \varepsilon_{yy} &= \varepsilon_{XX}\sin^2\varphi_{\rm SAW}, & \varepsilon_{xz} &= \varepsilon_{XZ}\cos\varphi_{\rm SAW}, \\ \varepsilon_{zz} &= \varepsilon_{ZZ}, & \varepsilon_{yz} &= \varepsilon_{XZ}\sin\varphi_{\rm SAW}, \end{aligned} \quad (2)$$

where $\varphi_{\rm SAW}$ is the angle between the SAW propagation direction and the crystallographic x axis parallel to the [100] direction.

Substituting Eq. (2) in Eq. (1), and considering that the equilibrium magnetization lies along the surface of the sample, the effective magnetoelastic field can be obtained as $\mu_0\mathbf{h} = -\nabla_m F_{\rm ME}$. It can be expressed as

$$\begin{aligned} \mu_0 h_{\rm ip} &= b_1\sin(2\varphi_0)\cos(2\varphi_{\rm SAW})\varepsilon_{XX} \\ &\quad - b_2\cos(2\varphi_0)\sin(2\varphi_{\rm SAW})\varepsilon_{XX}, \\ \mu_0 h_{\rm oop} &= 2b_2\cos(\varphi_0 - \varphi_{\rm SAW})\varepsilon_{XZ}, \end{aligned} \quad (3)$$

where $h_{\rm ip}$ and $h_{\rm oop}$ are the in-plane and out-of-plane effective fields, respectively, and φ_0 is the equilibrium direction of the magnetization with respect to the crystallographic x axis [100] as shown in Fig. 1. When the SAWs are perfectly aligned with the hard axis, $\varphi_{\rm SAW} = \pi/4$, both fields depend only on b_2. The term proportional to b_1 only contributes to $h_{\rm ip}$ when the SAW propagation direction deviates from the

hard axis. Moreover, in recent papers [49,50], a new driving field has been discussed whose orientation and angular dependence is the same as for h_{oop}. This field is attributed to magnetorotation (MR), which connects the rotation of the lattice with magnetic anisotropies. The equation of the effective MR field is $\mu_0 h_{\text{MR}} = -2K_u w_{XZ} \cos(\varphi_0 - \varphi_{\text{SAW}})$, where $w_{XZ} = 1/2(\partial u_X/\partial Z - \partial u_Z/\partial X)$ and $K_u = -1/2\mu_0 M_{\text{eff}}$ is the uniaxial out-of-plane anisotropy. Using the strain values given in Sec. III A, we obtain $\mu_0 h_{\text{ip}} = 0.1$ mT and $\mu_0 h_{\text{oop}} = 7 \times 10^{-4}$ mT. Regarding MR, the maximum value of w_{XZ} is found to be 5.5×10^{-5}, resulting in an effective MR field $\mu_0 h_{\text{MR}} = 0.06$ mT. This is two orders of magnitude larger than the ME h_{oop} field. However, our simulations show that, for $f_{\text{SAW}} = 500$ MHz, the magnetization dynamics is mostly determined by h_{ip} [51], so that we can neglect the contributions of both h_{oop} and h_{MR}.

The SAW strain is modeled as a propagating wave that depends on the amplitude and propagation direction as

$$\varepsilon_{jk}(r,t) = \varepsilon_{jk}^0 \exp(i(\mathbf{kr} - \omega t)), \tag{4}$$

where ε_{jk}^0 is the amplitude, $k = 2\pi/\lambda_{\text{SAW}}$ and $\omega = 2\pi f_{\text{SAW}}$ are the wave vector and the angular frequency of the SAW, respectively. We varied the strength of the applied magnetic field as well as the angle $\Delta\varphi_H$ from 0.5° up to 3°. We also took the magnetoelastic constants b_1 and b_2 as parameters.

The simulation involves sweeping the magnetic field as a function of time using the equation $\mu_0 H = \mu_0 H_0 t/t_{\text{max}}$, where $\mu_0 H_0$ is the final magnetic field (20 mT in this case) and t_{max} is the total simulation time. Therefore, the magnetic field goes from 0 to 20 mT, where each step of time corresponds to a step in magnetic field. The initial magnetic state is fixed at an easy axis and evolves to the magnetic state with minimum free energy for each magnetic field. Figure 5 gives a summary of the results, where the evolution of both equilibrium magnetization and oscillation amplitudes is plotted as a function of the applied magnetic field. Figure 5(a) shows the normalized magnetization of the oscillating signals for the magnetic components m_X and m_Y [coordinate system with a capital letter (X, Y, Z)] with each line color representing a different angle between the magnetic field and the SAW, $\Delta\varphi_H$. Both magnetization components start at cos(45°). As the magnetic field applied along the X direction approaches the anisotropy field, m_X tends to 1 and m_Y tends to 0. The inset in Fig. 5(a) shows the magnetization in the Y direction as a function of time and shows that the magnetization oscillates with a period of 2 ns corresponding to the SAW frequency of 500 MHz. Figure 5(b) shows the peak-to-peak amplitude of the m_Y component—equivalent to the component extracted from the spin waves in the XMCD images—as a function of the magnetic field, for different alignment angles between the magnetic field and the

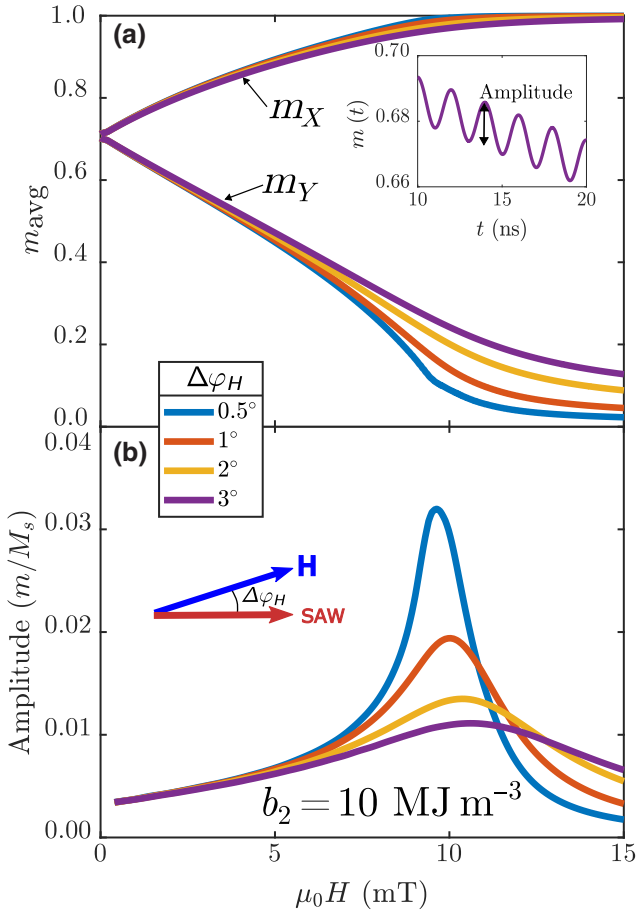

FIG. 5. (a) Average normalized magnetization components, m_X and m_Y, as a function of the magnetic field strength for several degrees of misalignment between the magnetic field and the SAW propagation direction. The inset shows the m_Y component as a function of time, and the amplitude is taken peak-to-peak. The value m_{avg} is the moving average of the time oscillation where each time step corresponds to a magnetic field step. (b) Amplitude of the normalized magnetic component m_Y (spin-wave amplitude) as a function of the magnetic field for different angles $\Delta\varphi_H$.

SAW, $\Delta\varphi_H$. The amplitude of the magnetization oscillation has the same behavior as that found from the XMCD experiment: a broad peak centered at the anisotropy field $\mu_0 H_k$ and a narrow 1 mT peak centered at the magnetic resonance close to 9–10 mT. We notice that as the angle of misalignment, $\Delta\varphi_H$, increases, the resonance peak disappears, and only the broad peak is left. This is due to the further shift of the spin-wave resonance curve for $\mathbf{q} = \mathbf{k}_{\text{SAW}}$ [41] away from the SAW frequency (500 MHz), and, similarly to absorption experiments, an angle $\Delta\varphi_H$ larger than 1.5° results in a negligible resonance coupling between SAWs and spin waves.

Finally, we investigated the dependence of the simulated curves on the values of the magnetoelastic constants b_1 and b_2. As mentioned previously, the term of the MR

field proportional to b_1 has a small effect on magnetization dynamics and therefore is fixed at $b_1 = 5$ MJ/m^3, while b_2 was swept from 0 to 14 MJ/m^3. The best agreement between simulations and experimental results falls in the range $b_2 = 10 \pm 4$ MJ/m^3. Figure 5(b) shows the results obtained for $b_2 = 10$ MJ/m^3. The simulations for $\Delta\varphi_H$ between 0.5° and 1° are in good agreement with our data from the XMCD-XPEEM experiment.

IV. DISCUSSION AND CONCLUSIONS

We have investigated the acoustic excitation of spin waves in hybrid structures consisting of a piezoelectric GaAs substrate and a ferromagnetic Fe_3Si thin film. We have directly imaged and quantified magnetoacoustic waves in Fe_3Si generated with SAWs and observed that magnetoacoustic waves are generated within a wide range of applied magnetic fields with a clear boost at magnetic resonance. The boost at the resonance field matches the FMR and SAW-FMR absorption peaks, indicating a larger energy transfer between the SAW and the magnetic system. However, we clearly observed magnetoacoustic waves at nonresonance fields, with less energy absorption. Thus, we conclude that resonance and energy absorption techniques do not provide a full picture of the magnetoacoustic dynamics in magnetic materials.

Further, XPEEM data allowed us to directly quantify the SAW strain components, and the amplitude of the SAW-induced spin waves was obtained from the corresponding XMCD images. Finally, through micromagnetic simulations, we have determined a range for the strength of the shear magnetoelastic constant ($b_2 = 10 \pm 4$ MJ/m^3) at 500 MHz.

The findings presented in this study offer valuable insights into the creation, detection, and manipulation of spin waves using SAWs. To date, magnetoelastic constants have primarily been determined using static measurements. Therefore, demonstrating that the dynamic magnetoelastic effect can also be utilized up to the gigahertz range for controlling magnetization dynamics with comparable efficiency to the static case underscores the potential of spin-wave-based devices as promising candidates for future information processing units. These devices offer the advantage of low-energy dissipation and compatibility with existing technologies.

ACKNOWLEDGMENTS

The authors would like to thank H.P. Schönherr and S. Meister for their technical support in the preparation of the samples. M.R., B.C., J.M.H., M.W.Q. and F.M. acknowledge funding from MCIN/AEI/10.13039/501100011033 through Grant No. PID2020-113024GB-100. M.F. and M.A.N. acknowledge funding from MCIN through Grants No. RTI2018-095303 and No. PID2021-122980OB-C54. M.W.K. acknowledges also Marie Skłodowska-Curie Grant No. 754397 (DOC-FAM) from EU Horizon 2020.

[1] Y. Li, W. Zhang, V. Tyberkevych, W.-K. Kwok, A. Hoffmann, and V. Novosad, Hybrid magnonics: Physics, circuits, and applications for coherent information processing, J. Appl. Phys. **128**, 130902 (2020).

[2] J. Inman, Y. Xiong, R. Bidthanapally, S. Louis, V. Tyberkevych, H. Qu, J. Sklenar, V. Novosad, Y. Li, X. Zhang, and W. Zhang, Hybrid Magnonics for Short-Wavelength Spin Waves Facilitated by a Magnetic Heterostructure, Phys. Rev. Appl. **17**, 044034 (2022).

[3] M. Foerster, F. Macià, N. Statuto, S. Finizio, A. Hernández-Mínguez, S. Lendínez, P. Santos, J. Fontcuberta, J. Hernàndez, M. Kläui, and L. Aballe, Direct imaging of delayed magneto-dynamic modes induced by surface acoustic waves, Nat. Commun. **8**, 407 (2017).

[4] P. Kuszewski, J.-Y. Duquesne, L. Becerra, A. Lemaître, S. Vincent, S. Majrab, F. Margaillan, C. Gourdon, and L. Thevenard, Optical Probing of Rayleigh Wave Driven Magnetoacoustic Resonance, Phys. Rev. Appl. **10**, 034036 (2018).

[5] M. Foerster, L. Aballe, J. M. Hernàndez, and F. Macià, Subnanosecond magnetization dynamics driven by strain waves, MRS Bull. **43**, 854 (2018).

[6] I. Bertelli, J. J. Carmiggelt, T. Yu, B. G. Simon, C. C. Pothoven, G. E. W. Bauer, Y. M. Blanter, J. Aarts, and T. van der Sar, Magnetic resonance imaging of spin-wave transport and interference in a magnetic insulator, Sci. Adv. **6**, eabd3556 (2020).

[7] B. Casals, N. Statuto, M. Foerster, A. Hernández-Mínguez, R. Cichelero, P. Manshausen, A. Mandziak, L. Aballe, J. M. Hernàndez, and F. Macià, Generation and Imaging of Magnetoacoustic Waves over Millimeter Distances, Phys. Rev. Lett. **124**, 137202 (2020).

[8] M. Kraimia, P. Kuszewski, J.-Y. Duquesne, A. Lemaître, F. Margaillan, C. Gourdon, and L. Thevenard, Time- and space-resolved nonlinear magnetoacoustic dynamics, Phys. Rev. B **101**, 144425 (2020).

[9] D. Labanowski, V. P. Bhallamudi, Q. Guo, C. M. Purser, B. A. McCullian, P. C. Hammel, and S. Salahuddin, Voltage-driven, local, and efficient excitation of nitrogen-vacancy centers in diamond, Sci. Adv. **4**, eaat6574 (2018).

[10] J. Hernandez, P. Santos, F. Macià, A. García-Santiago, and J. Tejada, Acoustomagnetic pulse experiments in $LiNbO_3/Mn_{12}$ hybrids, Appl. Phys. Lett. **88**, 012503 (2006).

[11] S. Davis, A. Baruth, and S. Adenwalla, Magnetization dynamics triggered by surface acoustic waves, Appl. Phys. Lett. **97**, 232507 (2010).

[12] M. Weiler, L. Dreher, C. Heeg, H. Huebl, R. Gross, M. S. Brandt, and S. T. B. Goennenwein, Elastically Driven Ferromagnetic Resonance in Nickel Thin Films, Phys. Rev. Lett. **106**, 117601 (2011).

[13] M. Weiler, H. Huebl, F. S. Goerg, F. D. Czeschka, R. Gross, and S. T. B. Goennenwein, Spin Pumping with Coherent Elastic Waves, Phys. Rev. Lett. **108**, 176601 (2012).

[14] P. G. Gowtham, T. Moriyama, D. C. Ralph, and R. A. Buhrman, Traveling surface spin-wave resonance spectroscopy using surface acoustic waves, J. Appl. Phys. **118**, 233910 (2015).

[15] D. Labanowski, A. Jung, and S. Salahuddin, Power absorption in acoustically driven ferromagnetic resonance, Appl. Phys. Lett. **108**, 022905 (2016).

[16] L. Thevenard, I. S. Camara, S. Majrab, M. Bernard, P. Rovillain, A. Lemaître, C. Gourdon, and J.-Y. Duquesne, Precessional magnetization switching by a surface acoustic wave, Phys. Rev. B **93**, 134430 (2016).

[17] P. Kuszewski, I. S. Camara, N. Biarrotte, L. Becerra, J. von Bardeleben, W. S. Torres, A. Lemaître, C. Gourdon, J.-Y. Duquesne, and L. Thevenard, Resonant magneto-acoustic switching: influence of Rayleigh wave frequency and wavevector, J. Phys. Condens. Matter **30**, 244003 (2018).

[18] M. Foerster and F. Macià, Preface to special issue on magneto-elastic effects, J. Phys. Condens. Matter **31**, 190301 (2019).

[19] J. Puebla, Y. Hwang, S. Maekawa, and Y. Otani, Perspectives on spintronics with surface acoustic waves, Appl. Phys. Lett. **120**, 220502 (2022).

[20] L. Dreher, M. Weiler, M. Pernpeintner, H. Huebl, R. Gross, M. S. Brandt, and S. T. B. Goennenwein, Surface acoustic wave driven ferromagnetic resonance in nickel thin films: Theory and experiment, Phys. Rev. B **86**, 134415 (2012).

[21] J. Walowski, M. D. Kaufmann, B. Lenk, C. Hamann, J. McCord, and M. Münzenberg, Intrinsic and non-local Gilbert damping in polycrystalline nickel studied by Ti:sapphire laser fs spectroscopy, J. Phys. D: Appl. Phys. **41**, 164016 (2008).

[22] G. Schmidt, C. Hauser, P. Trempler, M. Paleschke, and E. T. Papaioannou, Ultra thin films of yttrium iron garnet with very low damping: A review, Phys. Status Solidi (b) **257**, 1900644 (2020).

[23] J. Herfort, H.-P. Schönherr, A. Kawaharazuka, M. Ramsteiner, and K. Ploog, Epitaxial growth of Fe3Si/GaAs(001) hybrid structures for spintronic application, J. Cryst. Growth **278**, 666 (2005).

[24] A. Ionescu, C. A. F. Vaz, T. Trypiniotis, C. M. Gürtler, H. García-Miquel, J. A. C. Bland, M. E. Vickers, R. M. Dalgliesh, S. Langridge, Y. Bugoslavsky, Y. Miyoshi, L. F. Cohen, and K. R. A. Ziebeck, Structural, magnetic, electronic, and spin transport properties of epitaxial Fe_3Si/GaAs(001), Phys. Rev. B **71**, 094401 (2005).

[25] J. Herfort, H.-P. Schönherr, and K. H. Ploog, Epitaxial growth of Fe_3Si/GaAs(001) hybrid structures, Appl. Phys. Lett. **83**, 3912 (2003).

[26] D. Bas, P. Shah, A. Matyushov, M. Popov, V. Schell, R. Budhani, G. Srinivasan, E. Quandt, N. Sun, and M. Page, Acoustically driven ferromagnetic resonance in diverse ferromagnetic thin films, IEEE Trans. Magn. **PP**, 1 (2020).

[27] C. Gusenbauer, T. Ashraf, J. Stangl, G. Hesser, T. Plach, A. Meingast, G. Kothleitner, and R. Koch, Interdiffusion in heusler film epitaxy on GaAs(001), Phys. Rev. B **83**, 035319 (2011).

[28] J. Thomas, J. Schumann, H. Vinzelberg, E. Arushanov, R. Engelhard, O. G. Schmidt, and T. Gemming, Epitaxial Fe_3Si films on GaAs(100) substrates by means of electron beam evaporation, Nanotechnology **20**, 235604 (2009).

[29] K. Lenz, E. Kosubek, K. Baberschke, H. Wende, J. Herfort, H.-P. Schönherr, and K. H. Ploog, Magnetic properties of Fe_3Si/GaAs(001) hybrid structures, Phys. Rev. B **72**, 144411 (2005).

[30] K. Lenz, E. Kosubek, K. Baberschke, J. Herfort, H.-P. Schönherr, and K. H. Ploog, Magnetic anisotropy and resonance linewidth of Fe_3Si/GaAs(001), Phys. Status Solidi **3**, 122 (2006).

[31] M. Wegscheider, G. Käferböck, C. Gusenbauer, T. Ashraf, R. Koch, and W. Jantsch, Magnetic anisotropy of epitaxial $Fe_{1-x}Si_x$ films on GaAs(001), Phys. Rev. B **84**, 054461 (2011).

[32] J. B. Restorff, M. Wun-Fogle, K. B. Hathaway, A. E. Clark, T. A. Lograsso, and G. Petculescu, Tetragonal magnetostriction and magnetoelastic coupling in Fe-Al, Fe-Ga, Fe-Ge, Fe-Si, Fe-Ga-Al, and Fe-Ga-Ge alloys, J. Appl. Phys. **111**, 023905 (2012).

[33] B. A. Auld, *Acoustic Fields and Waves in Solids* (John Wiley and Sons, New York, 1973), Vol. 2.

[34] M. F. Lewis, in *Rayleigh-Wave Theory and Application* (Springer Berlin Heidelberg), p. 37.

[35] A. Hernández-Mínguez, F. Macià, J. M. Hernàndez, J. Herfort, and P. V. Santos, Large Nonreciprocal Propagation of Surface Acoustic Waves in Epitaxial Ferromagnetic/Semiconductor Hybrid Structures, Phys. Rev. Appl. **13**, 044018 (2020).

[36] M. Foerster, J. Prat, V. Massana, N. Gonzalez, A. Fontsere, B. Molas, O. Matilla, E. Pellegrin, and L. Aballe, Custom sample environment at the ALBA XPEEM, Ultramicroscopy **171**, 63 (2016).

[37] M. Foerster, N. Statuto, B. Casals, A. Hernández-Mínguez, S. Finizio, A. Mandziak, L. Aballe, J. M. Hernàndez Ferràs, and F. Macià, Quantification of propagating and standing surface acoustic waves by stroboscopic X-ray photoemission electron microscopy, J. Synch. Rad. **26**, 184 (2019).

[38] J. Stohr and H. Siegmann, *Magnetism: from Fundamentals to Nanoscale Dynamics* (Springer Berlin Heidelberg, Heidelberg, 2006), Vol. 152.

[39] V. Flovik, F. Macià, J. M. Hernàndez, R. Bručas, M. Hanson, and E. Wahlström, Tailoring the magnetodynamic properties of nanomagnets using magnetocrystalline and shape anisotropies, Phys. Rev. B **92**, 104406 (2015).

[40] See Supplemental Material note 1 at http://link.aps.org/supplemental/10.1103/PhysRevApplied.20.034052 for the results on the FMR experiment indicating the properties of the material.

[41] See Supplemental Material note 2 at http://link.aps.org/supplemental/10.1103/PhysRevApplied.20.034052 for the comparison between spin wave resonance and uniform mode resonance.

[42] J.-Y. Duquesne, P. Rovillain, C. Hepburn, M. Eddrief, P. Atkinson, A. Anane, R. Ranchal, and M. Marangolo, Surface-Acoustic-Wave Induced Ferromagnetic Resonance in Fe Thin Films and Magnetic Field Sensing, Phys. Rev. Appl. **12**, 024042 (2019).

[43] P. Rovillain, J.-Y. Duquesne, L. Christienne, M. Eddrief, M. G. Pini, A. Rettori, S. Tacchi, and M. Marangolo, Impact of

Spin-Wave Dispersion on Surface-Acoustic-Wave Velocity, Phys. Rev. Appl. **18**, 064043 (2022).

[44] See Supplemental Material note 3 at http://link.aps.org/supplemental/10.1103/PhysRevApplied.20.034052 for examples of spin wave patterns and fittings of the XMCD images.

[45] See Supplemental Material note 4 at http://link.aps.org/supplemental/10.1103/PhysRevApplied.20.034052 for information on how the magnetization is quantified from the XMCD images.

[46] A. Vansteenkiste, J. Leliaert, M. Dvornik, M. Helsen, F. Garcia-Sanchez, and B. Van Waeyenberge, The design and verification of MuMax3, AIP Adv. **4**, 107133 (2014).

[47] M. Szymanski, M. Jankowski, L. Dobrzynski, A. Wisniewski, and S. Bednarski, Spin dynamics of Fe_3Si and Fe_3-xMn_x alloys, J. Phys. Condens. Matter **3**, 4005 (1991).

[48] R. Sasaki, Y. Nii, Y. Iguchi, and Y. Onose, Nonreciprocal propagation of surface acoustic wave in Ni/$LiNbO_3$, Phys. Rev. B **95**, 020407 (2017).

[49] M. Xu, K. Yamamoto, J. Puebla, K. Baumgaertl, B. Rana, K. Miura, H. Takahashi, D. Grundler, S. Maekawa, and Y. Otani, Nonreciprocal surface acoustic wave propagation via magneto-rotation coupling, Sci. Adv. **6**, eabb1724 (2020).

[50] M. Küß, M. Heigl, L. Flacke, A. Hörner, M. Weiler, M. Albrecht, and A. Wixforth, Nonreciprocal Dzyaloshinskii–Moriya Magnetoacoustic Waves, Phys. Rev. Lett. **125**, 217203 (2020).

[51] See Supplemental Material note 5 at http://link.aps.org/supplemental/10.1103/PhysRevApplied.20.034052 for information on how the magnetization is quantified from the XMCD images.